

An Open Source, Massively Parallel Code for Non-LTE Synthesis and Inversion of Spectral Lines and Zeeman-induced Stokes Profiles

H. Socas-Navarro^{1,2}, J. de la Cruz Rodríguez³, A. Asensio Ramos^{1,2}, J. Trujillo Bueno^{1,2,4}, B. Ruiz Cobo^{1,2}

¹ Instituto de Astrofísica de Canarias, Avda Vía Láctea S/N, La Laguna 38205, Tenerife, Spain

² Departamento de Astrofísica, Universidad de La Laguna, 38205, La Laguna, Tenerife, Spain

³ Institute for Solar Physics, Dept. of Astronomy, Stockholm University, Albanova University Center, 10691 Stockholm, Sweden

⁴ Consejo Superior de Investigaciones Científicas, Spain

August 28, 2014

ABSTRACT

With the advent of a new generation of solar telescopes and instrumentation, the interpretation of chromospheric observations (in particular, spectro-polarimetry) requires new, suitable diagnostic tools. This paper describes a new code, NICOLE, that has been designed for Stokes non-LTE radiative transfer, both for synthesis and inversion of spectral lines and Zeeman-induced polarization profiles, spanning a wide range of atmospheric heights, from the photosphere to the chromosphere. The code fosters a number of unique features and capabilities and has been built from scratch with a powerful parallelization scheme that makes it suitable for application on massive datasets using large supercomputers. The source code is being publicly released, with the idea of facilitating future branching by other groups to augment its capabilities.

Key words. Radiative Transfer — Sun: chromosphere — Sun: photosphere — Sun: magnetic fields — Polarization — Sun: abundances

1. Introduction

The relevance of chromospheric line diagnostics has increased dramatically in the last decade among solar scientists. This is due to (or evidenced by, depending on how one looks at it) very significant advances in both numerical simulations and spectro-polarimetric observations. The largest instrumental projects for the next decades, namely the DKIST (formerly known as ATST, Keil et al. 2011; Keil et al. 2003), the EST (Collados et al. 2013; Collados et al. 2010) and Solar-C (Katsukawa et al. 2012; Shimizu et al. 2011) have all been designed with chromospheric magnetometry as a top priority. Moreover, several important modern facilities such as SOLIS (Bertello et al. 2013; Pevtsov et al. 2011), Gregor (Denker et al. 2012; Soltau et al. 2012), the SST with CRISP (Scharmer et al. 2003; Scharmer et al. 2008), the DST and the Big Bear NST (Cao et al. 2013; Goode & Cao 2012), foster remarkable chromospheric-observing capabilities.

Numerical simulations of the solar atmosphere have grown notably in size, scope and complexity (Stein 2012; Rempel & Schlichenmaier 2011). A particularly noteworthy effort in this context is the development of numerical MHD simulations of the magnetic chromosphere (Khomenko et al. 2014; Gudiksen et al. 2011). The simulated magnetic structures are still of relatively low field strengths, but this limitation is of technical nature. Hopefully, more processing power and new developments in numerical methods will permit higher flux densities in the near future.

Bridging the gap between the new ground-breaking observations and simulations requires complex modeling and diagnostic tools. NICOLE is a step in this direction. Capable of

Non-LTE (hereafter NLTE) spectral line calculations, it is suitable for the analysis of chromospheric lines and their polarization profiles in the Zeeman regime. The user is able to synthesize spectral profiles from large simulation datacubes, allowing a direct comparison with observations (it is possible to include the instrumental profile in the calculation). Conversely, the code inversion engine is able to work on the observed spectral data to infer relevant atmospheric parameters (such as temperatures, magnetic field vector or Doppler velocities) which may provide interesting information or be compared directly with the simulations. Other existing NLTE codes that share some (but not all) of NICOLE's features are HAZEL (Asensio Ramos et al. 2008), RH (Uitenbroek 2001) and Porta (Štěpán & Trujillo Bueno 2013).

NICOLE has been designed from the beginning to work on massive datasets, e.g. large simulation snapshots or high-resolution observations. The code implements a simple but efficient master-slave scheme using the widely available MPI (Message-Passing Interface) parallelization. This design makes it suitable for any architecture, including the most powerful supercomputers with over a thousand processors. With its 1.5D approach (meaning that each model column is treated as a horizontally-infinite atmosphere), almost ideal parallelization is achieved even for the largest number of processors.

The discussion presented in this section has been thus far focused on solar physics only but this tool is of great potential usefulness in other areas of astrophysics, as well. The code can easily provide flux-calibrated spectra of late-type stars. The capability for inversion of stellar spectra has been implemented following the work of Allende Prieto et al. (1998; see also Allende Prieto et al. 2000, 2001) and works similarly to

their code MISS. Chemical abundances may be inverted using NICOLE, as well, which might be an interesting capability for studies of solar/stellar compositions.

NICOLE has been released to the community as an open source project under the GPL license¹, which means that it may be copied, altered and redistributed, as long as any resulting product is also distributed openly to the community. Users are welcome, and in fact encouraged, to branch out their own version of NICOLE to improve it, augment it or to implement new features. The source code is currently hosted at the following repository: <https://github.com/hsocasnavarro/NICOLE>

2. Code description

Although NICOLE has been almost entirely written from scratch and incorporates many novel modules and elements, it builds upon previous experience with other very popular radiative transfer codes. The structure of the inversion mode in NICOLE is similar to that of SIR (Stokes Inversion based on Response-functions, Ruiz Cobo & del Toro Iniesta 1992). In the NLTE module, the structure and variable naming is similar to MULTI (Scharmer & Carlsson 1985). The NLTE iterative core is an implementation of the method described in Socas-Navarro & Trujillo Bueno (1997). The inversion module works in the same way as the code of Socas-Navarro et al. (1998, 2000). The following is a list of the approximations and limitations that have driven the design of NICOLE:

- Statistical equilibrium: The NLTE atomic populations are computed assuming instantaneous balance between all transitions going into and out of each atomic level. Effects such as time-dependent ionization are thus neglected in the synthesis (although it could have been previously incorporated in the computation of the model atmosphere in the synthesis mode). The tests presented in de la Cruz Rodríguez et al. (2012) support the validity of this assumption in a realistic scenario involving the inversion of Ca II lines. Furthermore, Leenaarts et al. (2012) point out that it is also a suitable strategy for H α synthesis, provided that the MHD model accounts for such time-dependent ionization. Nevertheless, there might be other situations in which this approximation would be less adequate.
- Complete angle and frequency redistribution (CRD): This approximation states that the frequency and direction of an emitted photon is independent of the frequency and direction of a previously absorbed one by the atomic system. Uitenbroek (1989) demonstrated that this approximation works very well for the Ca II infrared triplet lines. Other lines, such as Ca II H and K exhibit some significant discrepancies near the core (but not at the core itself), between CRD and full computations.
- Polarization induced by the Zeeman effect: NICOLE does not account for polarization produced by scattering processes or modified by the Hanle effect. It is therefore more suitable for application on Stokes I and V , and for all the Stokes profiles only when the magnetic field is strong enough (typically in active regions). Observing away from the solar limb also helps to reduce the possible influence of scattering and Hanle (de-)polarization on the linear polarization profiles.
- Field-free NLTE populations: The statistical equilibrium equations are solved neglecting the presence of a magnetic field. This is usually a good approximation since the lines are often much broader than the Zeeman splitting (Rees 1969).

- Hydrostatic equilibrium: This approximation is employed *only* in inversion mode and *only* for the computation of the density scale. It affects mostly the conversion of optical to geometrical depth and, to some extent, the background opacities. Otherwise, strong line profiles are usually rather insensitive to density and pressure changes.
- Blends: Spectral calculations (both syntheses and inversions) may include an arbitrary number of lines with the only limitation that all the NLTE lines must be of the same element. Line blends are treated consistently in the final formal solution, including their polarization profiles. However, the NLTE atomic level populations are computed without considering blends.
- Collisional damping: The code incorporates the classic Unsold formula (Unsold 1955) and the more recent formalism of Anstee & O'Mara (1995) and Barklem et al. (1998).
- 1.5D calculation: Although the code works with three dimensional datacubes, each column is treated independently, as if it were infinite in the horizontal direction. This approximation works well in LTE and when computing strong NLTE lines. The reason for the latter is that in the line core the opacity is so high that the photons have a short mean free path. Therefore, the populations are controlled by the environmental conditions in their immediate surroundings. A more quantitative assessment of this approximation has been presented in de la Cruz Rodríguez et al. (2012).
- Hyperfine structure: Lines with hyperfine structure may be seamlessly integrated in the spectral synthesis or inversion, simply by supplying the appropriate atomic data in the configuration file. However, this mode usually has a significant performance impact (e.g., Socas-Navarro 2014).
- Flexible node location: The inversion nodes for NICOLE may be specified manually by the user and do not need to be equispaced. This enables a more efficient distribution of nodes through the atmosphere, packing them more densely where more information is available and spreading them out in areas where the observations are less sensitive.
- Bezier-interpolant formal solvers: NICOLE implements a number of options for the formal solution method. A very interesting new routine is based on Bezier interpolation and makes the code more robust and stable. More details are provided in Section 5.1 below.

3. The equation of state

The equation of state (EoS) establishes one or more constraints that relate the various fundamental parameters defining the state of the plasma. Solving the EoS to determine physical variables, such as electron pressure, internal energy or the H $^-$ negative ion density, to name a few examples, is often a necessary intermediate step in a broad range of numerical codes for radiative transfer or MHD simulation. It is not trivial to solve the EoS when partial ionization and molecule formation are considered.

For the purposes of the calculations involved in NICOLE, the plasma state is defined by its temperature (T), gas density (ρ), gas pressure (P_g), electron pressure (P_e) and the following number densities, needed for the background opacities: neutral hydrogen atoms (H), protons (H $^+$), negative hydrogen ions (H $^-$), hydrogen molecules (H $_2$) and ionized hydrogen molecules (H $_2^+$). All of these parameters may be supplied as input if desired. Alternatively, one could supply two of them (temperature plus one of density, gas pressure or electron pressure) and NICOLE will use the EoS to solve for the rest. If the option to impose hydrostatic equilibrium is set, then only the temperature stratification

¹ <http://www.gnu.org/copyleft/gpl.html>

and the upper boundary condition for the electron pressure are needed. This is actually how the code works in inversion mode.

In NICOLE the solution of the EoS is divided in two, generally independent, steps. The first step computes the distribution of the various H populations (H , H^+ , H^- , H_2 , H_2^+). The second step deals with the relationship among the thermodynamical parameters (T , ρ , P_g and P_e). In both cases there are three different methods to solve the EoS in NICOLE that the user may choose from.

3.1. Full ICE solution

In order to determine the density of particles in the solar plasma we need to solve not only the atomic ionization system but also the chemical equilibrium among all the possible molecules. NICOLE implements the instantaneous chemical equilibrium (ICE) calculation of Asensio Ramos et al. (2003); Asensio Ramos & Socas-Navarro (2005), with a compilation of data for a total of 273 molecules. Obviously, dealing with such a large number of molecules results in a very demanding computation at each gridpoint, having to solve a non-linear system of 273 equations and unknowns. In addition to the computing time demanded by this approach, there is also the problem that sometimes the iteration fails to converge. Only a very small percentage of the points suffer this convergence issue but nevertheless it might still be problematic for some applications in which stability over a large number of calculations is a strict requirement. Therefore, two other options, faster and more stable, have been implemented as well.

3.2. Restricted ICE solution

This is basically the same as the full solution except that only two H molecules are considered, H_2 and H_2^+ . The calculation is then faster and more stable than the full ICE but it might still fail (albeit rarely) and is slower than the NICOLE option (see below).

3.3. The NICOLE method

We have developed a new procedure that avoids iteration and is therefore perfectly stable and faster than the previously discussed options. It is based on the realization that one needs to know only how much of the H is in molecular form to derive all other relevant parameters in a straightforward manner. We trained an artificial neural network (ANN) using a large database of (T, P_e, m) values for which we had previously solved the full ICE system with the 273 molecules. The third input parameter m characterizes the plasma metallicity (in a logarithmic scale), so that all elements heavier than $Z=2$ have their abundances scaled by this factor. The ANN and the algorithms are very similar to those described in Socas-Navarro (2003) and Socas-Navarro (2005). The training set was initially computed starting from a uniform distribution of T (between 1,500 and 10,000 K), m (between -1.5 and 0.5) and $\log(P_g)$ (between -3 and 6 with P_g in dyn cm^{-2}). We used this initial dataset to study some properties of the distribution but the actual ANN training was done using a more optimal set, as explained below.

Not surprisingly, the fraction of molecular H does not cover the entire parameter space in a uniform manner. Instead, it is saturated in large regions of the space and there is only a relatively narrow range of input values in which we actually need to perform the calculation. This can be seen in Fig 1 (left), which

shows the (T, P_e) space spanned by the training set. The populated region has values for which the fraction of molecular H is non-trivial. The empty space to the right is too hot for molecules to form and therefore all H is in atomic form. To the left, there are no (T, P_e) values consistent with our (T, P_g) distribution.

The results shown in Fig 1 (left panel) suggest that we do not need to train the ANN to operate in the full domain of the input parameters. We need to cover only the populated region seen in the figure. In this manner we not only decrease the required size of the training set but also improve the accuracy of a given ANN since it can become more specialized by operating on a smaller subspace. We therefore constructed a new, more optimal, training set that includes only points in the relevant range. After successfully training the ANN with these points, we reached an accuracy (measured as the standard deviation of the difference between the validation set and the ANN result) of $\sim 5 \times 10^{-3}$ (see right panel of Fig 1). Our ANN has four non-linear layers with 10 neurons per layer.

Once we know how much H is in the form of molecules, we use the Saha ionization equation to compute all the relevant populations. We stress that, even though this method only gives us the abundance of the H molecule, it has been computed taking into account all others with the full ICE procedure.

For the thermodynamical variables we have the following options:

3.4. The Wittman procedure

The first option is the method of Wittmann (1974), which in turn is an improvement over the one introduced by Mihalas (1974). It is the method implemented in the SIR code of Ruiz Cobo & del Toro Iniesta (1992). Only H molecules are considered here, thus removing the necessity for iterations and speeding up the computation of the total gas pressure P_g . With this procedure P_g is obtained directly from the pair of values (T, P_e) . The reverse process, i.e. obtaining P_e from (T, P_g) , requires iteration from an initial guess, which is slower and could potentially fail to converge. This method is a good approximation in most conditions except for very cool plasmas, such as those in a sunspot umbra, where other molecules might be important.

3.5. Artificial Neural Networks

It is possible to train a set of ANNs to solve for both P_e from (T, P_g) and P_g from (T, P_e) . However, this calculation is far less accurate than the calculation of the H molecular fraction explained above (at least using a similar sized ANN). Figure 2 shows the spread in the validation set. The error in the logarithm of the retrieved pressure is of the order of 15%. On the other hand, there are many applications in which an accurate solution of the EoS is not required, since spectral lines are far less sensitive to density or gas pressure than they are to temperature. If the penalty in accuracy is acceptable then this method is by far the fastest and provides a direct solution in both directions.

3.6. NICOLE EoS

This is essentially the same procedure as the NICOLE method described above, using an ANN to determine the fraction of molecular H, but then solving the Saha ionization equation for the rest of atomic species to determine the electron number densities. The reverse process, i.e. obtaining P_g from (T, P_e) is done by iteration, just as in the Wittmann procedure.

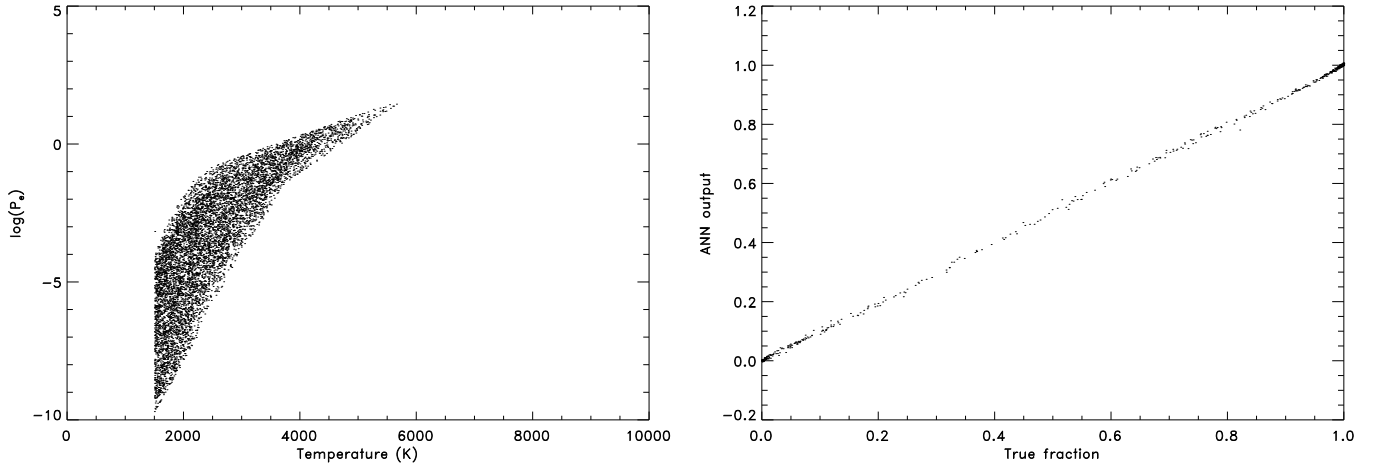


Fig. 1. Left: Points in our initial training set that exhibit a number fraction of molecular H greater than 0.1 and smaller than 0.9. Right: Scatter plot showing the accuracy of the ANN trained to retrieve the fraction of atomic H from $(T, P_e$ and $m)$. The standard deviation is $\sim 5 \times 10^{-3}$.

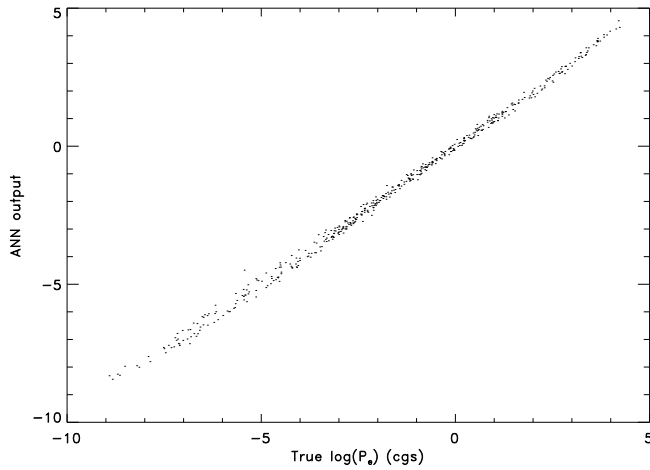


Fig. 2. Scatter plot showing the accuracy of the ANN trained to retrieve the logarithm of P_e from from $(T, P_g$ and $m)$. The standard deviation is $\sim 15\%$.

4. Background opacities

Background opacities are those resulting from continuum absorption processes, typically atomic photoionization. We distinguish two distinct wavelength regimes that are treated differently: ultraviolet and visible/infrared. The transition between those two regimes is located at 400 nm.

4.1. Visible and infrared opacities

NICOLE contains three different opacity packages for the calculation of background opacities in the visible and infrared. They account for almost the same physical processes (with the slight differences that we detail below) and therefore differ mostly in details such as the tabulated values employed or the actual coding.

4.1.1. The Wittmann package

This package computes continuum opacities due to H^- , neutral H, He^- , H_2^- , H_2^+ , photoionization of Ca, Na and Mg, and

Rayleigh scattering by neutral H, H_2 , neutral He and Thomson scattering by electrons. For more details see Wittmann (1974).

4.1.2. The SOPA package

We implemented a module with the background opacity package of Kostik et al. (1996), which includes neutral H, H^- , H_2^+ , photoionizations from the first 8 levels of Si, C, Mg, Al, and the first two levels of Fe, Rayleigh scattering by neutral H and Thomson scattering by free electrons. Unfortunately we were not able to bring this package to the coding standards of the NICOLE requirements. In order to avoid compile problems or hardware incompatibilities this package is not supported. It is disabled by default and available only via a special compilation-time switch for advanced users.

4.1.3. The NICOLE package

We developed an independent opacity package for NICOLE that computes opacities from neutral H, H^- and Mg, as well as scattering due to H, H_2 and free electrons.

Figures 3 and 4 compare the wavelength dependence of the background opacities computed by all three packages. Since this comparison depends strongly on the atmospheric conditions, we have chosen two sets of parameters.

4.2. Ultraviolet opacities

Computation of background opacities in the ultraviolet is far more complicated than in the visible. Many metallic species can undergo photoionization processes with sufficiently large cross-sections to become important opacity contributors in spite of their relatively low abundances. To complicate the matter further, there is not a dominant species above the 91 nm regime, where the H photoionization occurs. Depending on the prevailing conditions and the wavelength range, we are dominated by different metals. In addition to the SOPA package (see above), which includes some photoionization processes for a few interesting metals, we have two other packages in NICOLE specifically implemented for the computation of ultraviolet opacities.

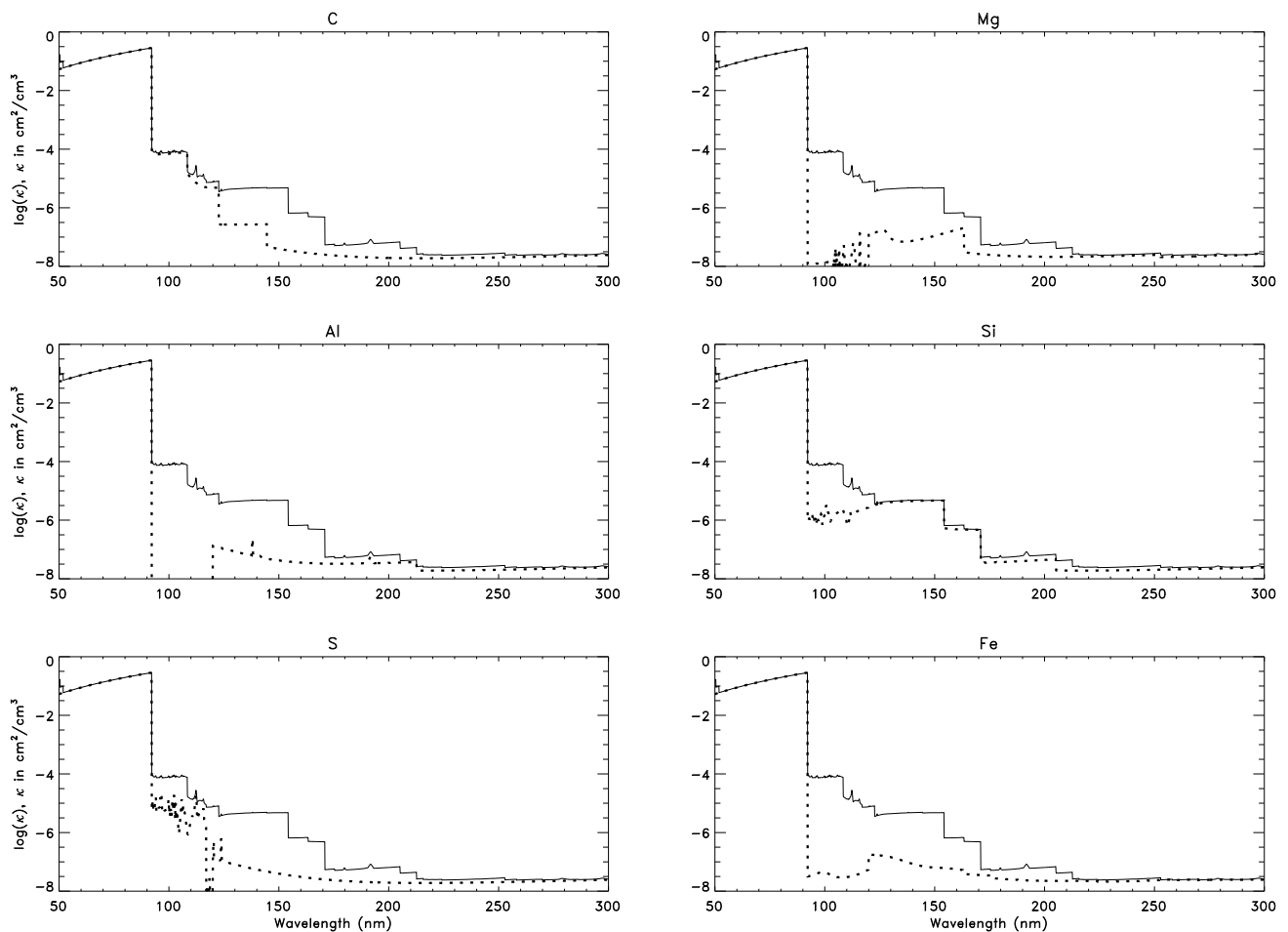


Fig. 7. Contribution of the most relevant metals to the background ultraviolet opacity in typical photospheric conditions ($T=5600$ K, $P_e=10$ dyn cm $^{-2}$, $P_g=8\times 10^5$ dyn cm $^{-2}$). Other elements become relevant under different conditions. Solid: Total opacity. Dotted: Resulting opacity when neglecting all metals except for the one indicated in the title of each plot.

4.2.1. The Dragon-Mutschlechner package

Dragon & Mutschlechner (1980) provide a set of tables to compute photoionization cross-sections for various levels of neutral Mg, Al, Si and Fe. Using some simple analytical expressions, we can obtain a rather good approximation in most practical situations (see Figures 5 and 6 below).

4.2.2. The TIP-TOP package

The Iron Project (TIP) and The Opacity Project (TOP) are two large collaborations aimed at producing the most comprehensive compilation of atomic opacity sources. The two projects started off as independent initiatives but have now joined forces and have published their tables with a large number of photoionization cross-sections for most metals. We have included all the available data for neutral and singly ionized elements between $Z=1$ and $Z=26$. In the particular case of the Fe atom, we use the data provided by Bautista (1997) and by Nahar & Pradhan (1994). In all cases the data are smoothed as discussed in Bautista et al. (1998); Allende Prieto et al. (2003); Allende Prieto (2008).

To make the problem tractable, NICOLE preloads in memory a large matrix with all the cross-sections (for each element and level) at each wavelength, discretized with a 0.1 nm sampling. When the opacity routine is called for a certain wave-

length and input conditions, it simply picks from the matrix all the cross-sections at that wavelength (rounded off to the closest point in the grid), weighs each one according to element abundance, ionization fraction and level excitation, and finally returns the total of all the contributors. With this strategy, we can obtain the total opacity from all contributors in the comprehensive TIP-TOP database in a very short time.

Figures 5 and 6 compare the various ultraviolet opacity packages in two different situations. In the photosphere (Fig 5), the TIP-TOP package yields a much more detailed curve with a plethora of peaks and discontinuities caused by photoionization from countless levels of several elements. The other two packages, however, produce a good smoothed out approximation. Under these atmospheric conditions, the opacity is dominated by neutral species. Under the chromospheric conditions of Fig 6, the opacity structure is much simpler. It is dominated by Thomson scattering on free electrons at all but the shortest wavelengths. Under these conditions we start to find some non-negligible contributions from ionized metals.

5. Formal solutions

Inside each vertical column, NICOLE solves the NLTE problem in 1D by assuming plane-parallel geometry, isotropic scattering and complete frequency redistribution (details in Socas-Navarro & Trujillo Bueno 1997). To compute the atom

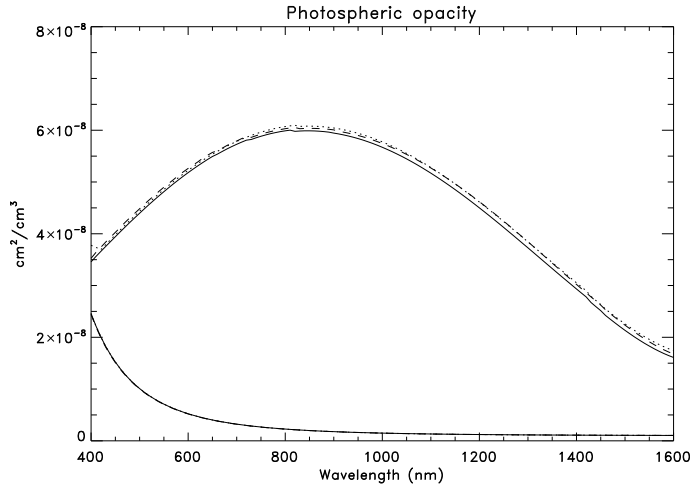


Fig. 3. Background opacities as a function of wavelength in typically photospheric conditions ($T=5600$ K, $P_e=10$ dyn cm $^{-2}$, $P_g=8\times 10^5$ dyn cm $^{-2}$). Solid line: Using the Wittmann package. Dashed line: Using the NICOLE package. Dotted line: Using the SOPA package. The lower curve represents the scattering contribution to the opacity (all three packages yield the same result within the line thickness of the plot). The scattering curve has been multiplied by a factor 100 for better visibility in this plot.

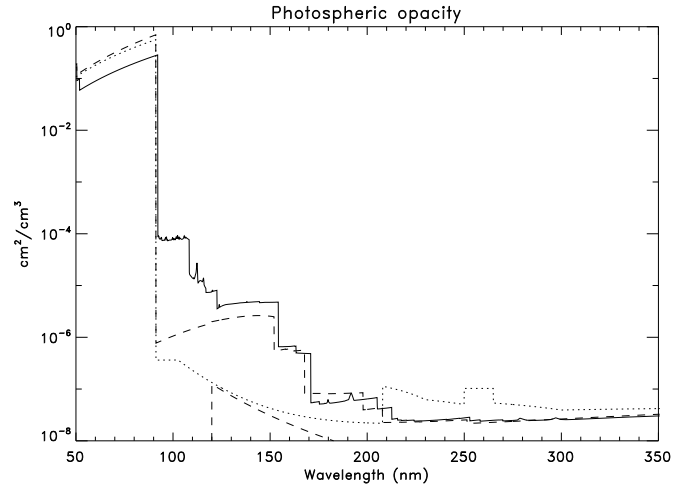


Fig. 5. Ultraviolet background opacities as a function of wavelength in typically photospheric conditions ($T=5600$ K, $P_e=10$ dyn cm $^{-2}$, $P_g=8\times 10^5$ dyn cm $^{-2}$). Solid line: Using the TIP-TOP package. Dashed line: Using the Dragon-Mutschlechner package. Dotted line: Using the SOPA package. The lower dashed curve represents the scattering contribution to the opacity (all three packages yield the same result within the line thickness of the plot).

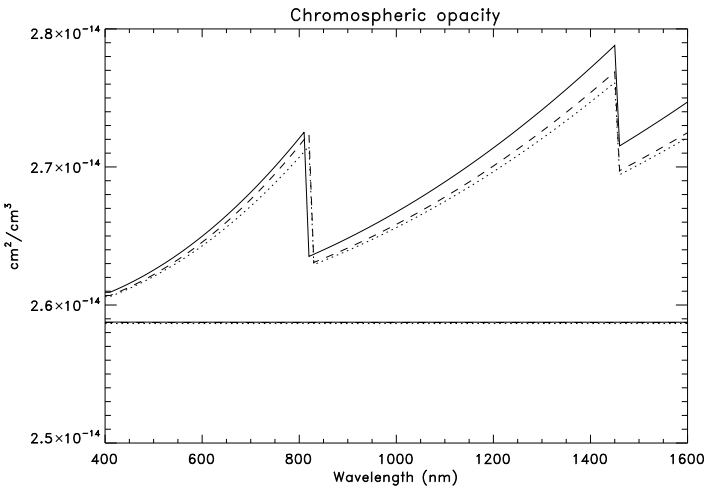


Fig. 4. Background opacities as a function of wavelength in typically chromospheric conditions ($T=9000$ K, $P_e=0.05$ dyn cm $^{-2}$, $P_g=0.15$ dyn cm $^{-2}$). Solid line: Using the Wittmann package. Dashed line: Using the NICOLE package. Dotted line: Using the SOPA package. The lower curve represents the scattering contribution to the opacity (all three packages yield the same result within the line thickness of the plot).

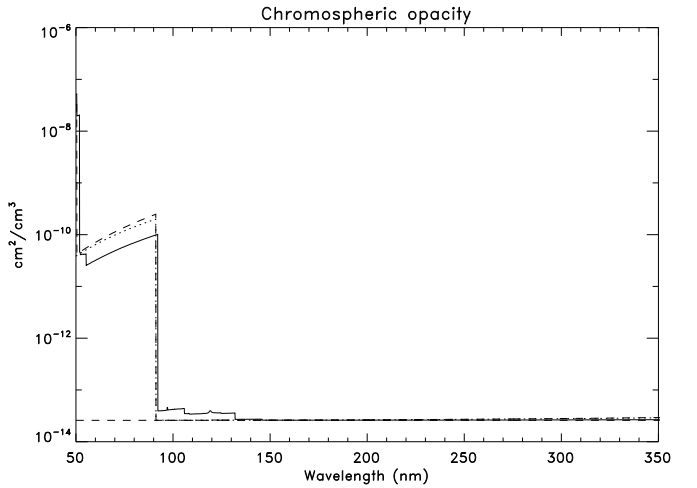


Fig. 6. Ultraviolet background opacities as a function of wavelength in typically chromospheric conditions ($T=9000$ K, $P_e=0.05$ dyn cm $^{-2}$, $P_g=0.15$ dyn cm $^{-2}$). Solid line: Using the TIP-TOP package. Dashed line: Using the Dragon-Mutschlechner package. Dotted line: Using the SOPA package. The lower dashed curve represents the scattering contribution to the opacity (all three packages yield the same result within the line thickness of the plot).

population densities, it assumes statistical equilibrium and unpolarized light. Once the populations are known, the full-Stokes vector is computed for Zeeman-induced polarization. Therefore, all Zeeman sublevels originating from a given atomic level are assumed to be equally populated, discarding any quantum interference between them (the *polarization-free* approximation, Trujillo Bueno & Landi Degl'Innocenti 1996).

5.1. Formal solutions and the NLTE problem

The radiative transfer equation for unpolarized light can be expressed as:

$$\frac{dI_\nu}{d\tau_\nu} = I_\nu - S_\nu, \quad (1)$$

where I_ν is the emerging intensity at frequency ν , τ_ν is the optical depth and S_ν is the source function. In a discrete grid of depth points where the subindexes u , o and d indicate the upwind point, central point and downwind point respectively, the solution to

Eq. 1 on the interval (τ_o, τ_u) is:

$$I(\tau_o) = I(\tau_u)e^{-\delta_o} + \int_{\tau_o}^{\tau_u} e^{-(\tau-\tau_o)} S(\tau) d\tau, \quad (2)$$

where $\delta_o \equiv \delta\tau_o = |\tau_u - \tau_o|$. To integrate analytically Eq. (2), the source function can be approximated using a polynomial interpolant: linear, quadratic, etc. We have implemented two formal solutions of the radiative transfer equation (methods) to compute the atom population densities (unpolarized), based on short-characteristics:

1. The source function is approximated with a parabolic interpolant, centered in the grid point where the intensity is being calculated (Olson & Kunasz 1987). This interpolant behaves particularly well on equidistant grids, but it is known to overshoot in irregular grids. Therefore, when overshooting is detected, we adopt a linear approximation instead.
2. An elegant approach, introduced by Auer (2003), is to use Bezier-splines interpolants. Bezier-splines provide a powerful framework to control overshooting, while keeping the accuracy of high-order interpolants. These methods have been implemented in 3D MHD codes (e.g., BIFROST, Hayek et al. 2010) and radiative transfer codes (e.g., Multi3d, PORTA, Leenaarts & Carlsson 2009; Štěpán & Trujillo Bueno 2013).

In particular, we have experimented extensively with the election of an appropriate diagonal approximate lambda operator and the treatment of overshooting cases in Method 2. The quadratic Bezier interpolant is defined using normalized abscissa units in the interval (x_o, x_u) :

$$u = \frac{x - x_u}{x_o - x_u},$$

so,

$$f(x) = y_u u^2 + y_o (1 - u)^2 + 2u(1 - u) \cdot C, \quad (3)$$

where C is a control point defined as:

$$C = S_o - \frac{\delta_o}{2} \frac{dS_o}{d\tau}. \quad (4)$$

The solution to Eq. 2, can be formulated in two ways. One is to re-arrange the terms of the integral so we get terms that only depend on the values of the source function in the upwind point (u), downwind point (d) and central point (o), by explicitly replacing the Eq. 4 into Eq. 3 before the integral in Eq. 2 is performed:

$$I_o = I_u e^{-\delta_o} + \alpha S_u + \beta S_o + \gamma S_d, \quad (5)$$

where α, β, γ are the interpolation coefficients. This is the choice of Hayek et al. (2010), therefore they choose an expression for computing numerically $dS_o/d\tau$ that linearly depends on S_u, S_o, S_d . However, de la Cruz Rodríguez & Piskunov (2013) and Štěpán & Trujillo Bueno (2013) express the solution as a function of S_u, S_o, C :

$$I_o = I_u e^{-\delta_o} + \hat{\alpha} S_u + \hat{\beta} S_o + \hat{\gamma} C. \quad (6)$$

In principle, both formalisms should be equivalent. The only difference appears when computing the diagonal approximate lambda operator (details in Olson & Kunasz 1987). To define the approximate lambda operator, one can use a source function that is set to zero at all depth points except $S_o = 1$, and check

what terms remain in Equation 5 and 6. Note that we are strictly neglecting the contribution from the ensuing intensity through the term $I_u e^{-\delta_o}$, which is typically very small in the optically thick regime (van Noort et al. 2002).

The implementation by Hayek et al. (2010) implicitly includes the terms used to compute $dS_o/d\tau$ in their operator, whereas the second formalism does not. It is straightforward to see that those terms appear because the derivative is computed numerically, but there is no reason to include them in the approximate operator. Also, by using the second formalism, it does not matter so much what expression is used for the derivative, given that the control point is not explicitly split into terms that depend on S_d, S_o and S_u (Auer 2003, proposes two different ways of computing centered derivatives). Our tests show that defining the local operator as $\Lambda^* = \hat{\beta} + \hat{\gamma}$ is optimal and convergence is achieved in less iterations.

Overshooting is suppressed by changing the value of the control point C as described in Hayek et al. (2010). The basic idea is to identify extrema in the source function, and to constrain the value of the control point within S_u and S_o . An important refinement is proposed by Štěpán & Trujillo Bueno (2013), who also check for overshooting in the downwind interval, between S_o and S_d . The latter indeed improves the stability of the solution, forcing the Bezier interpolant to approach point o monotonically in every situation.

So far, we have not mentioned much about Method 1. The problem is that allowing the solution to switch from parabolic to linear and vice-versa can lead to a flip-flop behaviour. Normally, more iterations are needed to reach a similar convergence threshold with this method than with the Bezier alternative.

5.2. Formal solution of the polarized transfer equations

Once the level populations are calculated, NICOLE allows to compute the emerging Stokes vector assuming Zeeman-induced polarization. We have implemented a list of formal solvers that can be used for this matter. The following alternatives are available:

- Quadratic and cubic DELO-Bezier (de la Cruz Rodríguez & Piskunov 2013).
- DELO-Linear (Rees et al. 1989).
- DELO-Parabolic (Trujillo Bueno 2003).
- Hermitian (Bellot Rubio et al. 1998).
- Weakly-polarizing media (Sánchez Almeida & Trujillo Bueno 1999).

6. Hyperfine structure

Almost every element in the periodic table has an isotope with non-zero nuclear angular momentum I , which couples with the sum of the orbital and spin angular momentum J . Consequently, the fine structure levels, characterized by their value of J , are split into hyperfine structure levels following the standard rule for angular momentum addition, yielding $F = |J - I| \dots J + I$. The hyperfine splitting is usually much smaller than the fine structure splitting. Thus, the presence of a weak magnetic field may be able to produce Zeeman splittings that are of the order of the energy level separation between consecutive F levels. Under these circumstances, the non-diagonal terms in the Zeeman Hamiltonian become of importance. This regime of intermediate Paschen-Back effect (or Back-Goudsmit effect) leads to strong perturbations on the Zeeman patterns, which may have an important impact on the emergent Stokes profiles.

The energy splitting of these F levels with respect to the original J level (the fine structure level without hyperfine structure) is given, with very good approximation, by Casimir (1963):

$$\Delta_{\text{HFS}}(J, F, I) = \frac{1}{2}AK + \frac{1}{2}B \frac{(3/4)K(K+1) - I(I+1)J(J+1)}{I(2I-1)J(2J-1)}, \quad (7)$$

where

$$K = F(F+1) - I(I+1) - J(J+1). \quad (8)$$

The energy splitting is represented in cm^{-1} when the constants A and B are given in cm^{-1} . These constants are the magnetic-dipole (A) and electric-quadrupole (B) hyperfine structure constants, and are characteristic of a given fine structure level. In the case that the energy level separation between consecutive fine structure levels is very large in comparison to the typical Zeeman splitting produced by the magnetic fields we are interested in, one may focus exclusively on the coupling between the hyperfine and magnetic interactions. The total Hamiltonian is block-diagonal and each block can be written as (e.g., Landi Degl'Innocenti & Landolfi 2004):

$$\begin{aligned} \langle (LS)JIFM_F | H | (LS)JIF'M'_F \rangle &= \delta_{FF'} \delta_{M_F M'_F} \Delta_{\text{HFS}}(J, F, I) \\ &+ \delta_{M_F M'_F} \mu_0 B g_J (-1)^{J+I-M_F} \sqrt{J(J+1)(2J+1)(2F+1)(2F'+1)} \\ &\times \begin{Bmatrix} F' & F & 1 \\ J & J & I \end{Bmatrix} \begin{pmatrix} F & F' & 1 \\ -M_F & M_F & 0 \end{pmatrix}, \end{aligned} \quad (9)$$

where μ_0 is the Bohr magneton, B is the magnetic field strength and g_J is the Landé factor of the level in L-S coupling.

The total Hamiltonian is diagonal in M_F , so that it remains a good quantum number even in the presence of a magnetic field. This is not the case with F , because the total Hamiltonian mixes levels with different values of F . After a numerical diagonalization of the Hamiltonian, the eigenvalues are associated with the energies of the M_F magnetic sublevels. The transition between the upper and lower fine structure levels produce many allowed transitions following the selection rules $\Delta M_F = 0, \pm 1$. The strength of each component can be obtained by evaluating the squared matrix element of the electric dipole operator (Landi Degl'Innocenti & Landolfi 2004):

$$S_q^{iM_F, i'M'_F} \propto |\langle (LS)JiM_F | r_q | (LS)Ji'M'_F \rangle|^2, \quad (10)$$

where $q = M_F - M'_F = 0, \pm 1$ and $\langle (LS)JiM_F \rangle$ are the eigenvectors of the Hamiltonian. The symbol i is used for identification purposes since F is not a good quantum number (e.g., Landi Degl'Innocenti & Landolfi 2004).

7. Abundance inversions

When working in inversion mode, it is possible to set element abundances as ‘‘inversion nodes’’. In this manner, NICOLE can be used in studies of solar and stellar chemical compositions, similarly to the MISS code of Allende Prieto et al. (2001). In principle it is possible to invert abundances and atmospheric parameters simultaneously. However, it is important to realize that doing this would only produce meaningful results if the observations include lines from multiple elements that can univocally constrain both the atmosphere and the composition. In general, it is better to have independent observations to determine the atmospheric model, or at least to have a good approximation to it before attempting to invert abundances.

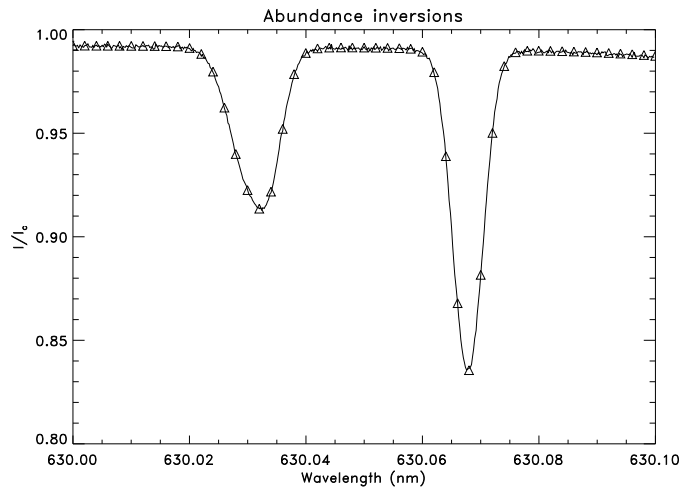


Fig. 8. Simulated inversion of three element abundances: O, Ni and Sc

Figure 8 shows a simulated inversion of the well-known blend of Ni I with a forbidden O I transition at 6300.3 \AA along with the nearby Sc II line. These lines have been frequently used in recent studies of the solar chemical composition, as this region has proven to be a valid diagnostics to resolve the so-called solar Oxygen crisis (e.g., Socas-Navarro 2014 and references therein). The simulated observations were synthesized with the HSRA quiet Sun model (Gingerich et al. 1971), adding random noise of a $1\text{-}\sigma$ amplitude of 5×10^{-4} . The reference abundances chosen in this test for the lines in the figure are 8.83, 6.25 and 3.17 (O, Ni and Sc, respectively). The inversion was initialized with highly discrepant values: 8.00, 5.50 and 4.00 and repeated up to 30 times adding a random perturbation of up to ± 0.2 dex to the reference values. Only 8 out of the 30 inversions converged to the correct solution, producing a fit down to the noise level. The fit shown in the figure is representative of these 8 solutions, having a χ^2 value that is approximately that of their average. The mean value and standard deviation of the results from the inversions are 8.835 ± 0.004 , 6.254 ± 0.004 and 3.174 ± 0.004 , respectively.

It is important to note that these extremely small uncertainties represent only the inversion error. In this case the model atmosphere is prescribed and known *a priori* because we are interested here in the error produced by the inversion process and the algorithm’s ability to find the correct solution. Otherwise, one would also have systematic errors arising from the atmospheric model uncertainty, which are likely much larger.

8. Parallelization

NICOLE was designed to work on large datasets, typically inversions of spectral (or, in general, spectro-polarimetric) scans of a 2D field of view (de la Cruz Rodríguez et al. 2013b) or spectral synthesis in simulation datacubes (Socas-Navarro 2014). For such applications, an efficient parallelization scheme is required. We have implemented a master-slave approach in which each slave works on a given spatial pixel. All input and output tasks are handled by the master process, which reads the input files, sends the input data to each idle slave, collects the computation results and finally writes them to disk. This strategy eliminates possible disk access conflicts or bottlenecks among processes and is optimal in minimizing the computing time for large problems. We achieve the goal of ideal parallelization, in which the CPU time is inversely proportional to the number of processors

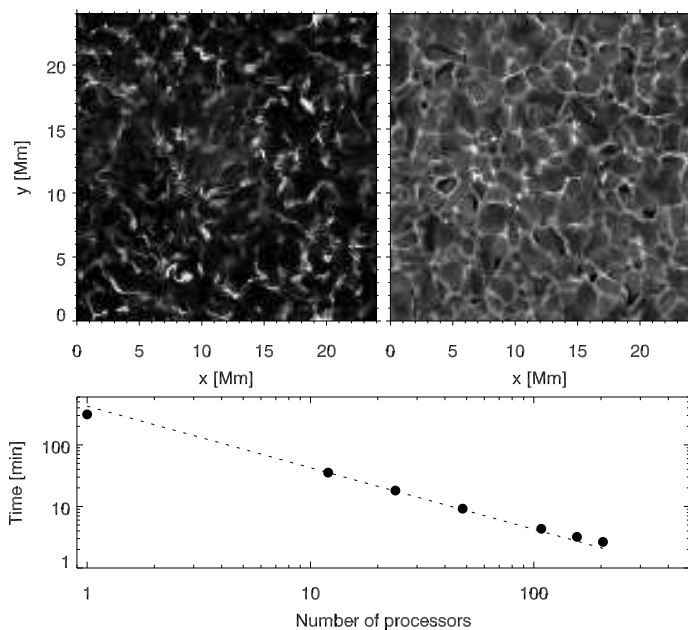


Fig. 9. *Top row:* Synthetic observations in the 854.2 nm line, close to line center (left panel) and in the extended photospheric wing (right panel). *Bottom:* CPU time as a function of the inverse number of processors. The dotted line represents the behavior expected for ideal parallelization.

(as long as the computation time is much longer than the time it takes to read the input data). This ideal parallelization holds independently of the number of processors, making NICOLE a massively parallel code which could potentially run efficiently even on the largest supercomputers with thousands of processors. We present some tests below demonstrating this good behavior up to 200 processors.

We conducted a series of tests with a benchmark calculation using the 3D MHD model computed with the BIFROST code (see Gudiksen et al. 2011). The snapshot used in our calculations is publicly available as part of the LMSAL IRIS mission data (De Pontieu et al. 2014) and has been previously used in a number of studies (e.g., Leenaarts et al. 2012; de la Cruz Rodríguez et al. 2013a; Pereira et al. 2013). The simulation is computed on a grid of $(x,y,z)=504\times 505\times 496$ points, corresponding to a physical size of approximately 24×24 Mm in the (x,y) -plane. Vertically, the simulation extends from 2.2 Mm below the photosphere, to 15 Mm above, and it encloses a photosphere, chromosphere and corona. We have only considered every 4th pixel in the horizontal (x,y) -plane to be able to perform the calculation with a reduced number of CPUs in our tests.

For each column in the simulation, we solved the NLTE problem with a 6-level Ca II atom and computed intensity and polarization profiles in the 8542 Å line. The hardware platform is a Linux AMD Opteron cluster with 524 cores. We employed a homogeneous subset of 204 of them in our tests (this cluster has several different processor models). Fig 9 shows a log-log plot of the total CPU time versus the inverse of the number of (slave) processors employed. In the ideal case of optimal parallelization one would expect a straight line whose slope is -1 and the abscissa at origin is the number of columns multiplied by the computing time per column. The figure shows that the tests follow this ideal behavior (represented in the dashed line), with no signs of saturation even at 200 processors.

Our parallelization is implemented using the MPI library. It is straightforward to compile and run the parallel version of NICOLE on any system with a working MPI installation. Since one of the processes is the master, it is usually more efficient to run NICOLE with $N + 1$ threads, where N is the number of available hardware processor cores.

9. Conclusions

NICOLE is the result of a multiyear effort to produce a public, well-documented, user-friendly code for massive radiative transfer calculations. It may be used in LTE or NLTE, to convert atmospheric models between geometrical and optical depth or to make inversions of observed profiles. It may be applied to solar or stellar models and observations. Interested researchers are invited to download the code from the link above and encouraged to make and redistribute any changes or modifications they deem necessary (permissions are explicitly granted under the GNU public license).

We expect that codes like NICOLE will become an important tool in the coming years, at least within the solar community. The advent of new instrumentation designed for chromospheric magnetometry will produce enormous datasets of NLTE spectral profiles that will require inversion. Additionally, state-of-the-art 3D numerical simulations of the solar atmosphere, spanning the whole range from the photosphere to the transition region, are becoming available and increasingly realistic. Polarized spectral synthesis in the simulation datacubes are necessary for the detailed comparison between simulations and observations.

NICOLE has already been tested and publications exist demonstrating its performance in inverting Stokes profiles in LTE (Socas-Navarro 2011), NLTE (de la Cruz Rodríguez et al. 2012; de la Cruz Rodríguez et al. 2013b; Leenaarts et al. 2014) and synthesizing large numbers of profiles in 3D atmospheric models (Socas-Navarro 2014).

A significant fraction of the NICOLE development effort has been directed to making this code as user-friendly as possible. However, it is important to remember that NICOLE, like any other complex numerical code, cannot be used as a black box. Understanding not only the underlying physics, but also the numerical procedures and the data products involved, is of paramount importance in order to obtain meaningful scientific results.

Acknowledgements. The authors thankfully acknowledge the technical expertise and assistance provided by the Spanish Supercomputing Network (Red Española de Supercomputación), as well as the computer resources used: the La-Palma Supercomputer, located at the Instituto de Astrofísica de Canarias. Financial support by the Spanish Ministry of Science and Innovation through project AYA2010-18029 (Solar Magnetism and Astrophysical Spectropolarimetry) is gratefully acknowledged. AAR also acknowledges financial support through the Ramon y Cajal fellowship.

References

- Allende Prieto, C. 2008, *Physica Scripta Volume T*, 133, 014014
- Allende Prieto, C., Barklem, P. S., Asplund, M., & Ruiz Cobo, B. 2001, *ApJ*, 558, 830
- Allende Prieto, C., García López, R. J., Lambert, D. L., & Ruiz Cobo, B. 2000, *ApJ*, 528, 885
- Allende Prieto, C., Lambert, D. L., Hubeny, I., & Lanz, T. 2003, *ApJS*, 147, 363
- Allende Prieto, C., Ruiz Cobo, B., & García López, J. 1998, *ApJ*, 502, 951
- Anstee, S. D. & O'Mara, B. J. 1995, *MNRAS*, 276, 859
- Asensio Ramos, A. & Socas-Navarro, H. 2005, *A&A*, 438, 1021
- Asensio Ramos, A., Trujillo Bueno, J., Carlsson, M., & Cernicharo, J. 2003, *ApJ*, 588, L61

- Asensio Ramos, A., Trujillo Bueno, J., & Landi Degl'Innocenti, E. 2008, *ApJ*, 683, 542
- Auer, L. 2003, in *Astronomical Society of the Pacific Conference Series*, Vol. 288, *Stellar Atmosphere Modeling*, ed. I. Hubeny, D. Mihalas, & K. Werner, 3
- Barklem, P. S., Anstee, S. D., & O'Mara, B. J. 1998, *PASA*, 15, 336
- Bautista, M. A. 1997, *A&AS*, 122, 167
- Bautista, M. A., Romano, P., & Pradhan, A. K. 1998, *ApJS*, 118, 259
- Bellot Rubio, L. R., Ruiz Cobo, B., & Collados, M. 1998, *ApJ*, 506, 805
- Bertello, L., Callahan, L., Gusain, S., et al. 2013, in *AAS/Solar Physics Division Meeting*, Vol. 44, *AAS/Solar Physics Division Meeting*
- Cao, W., Goode, P. R., & NST Team. 2013, in *AAS/Solar Physics Division Meeting*, Vol. 44, *AAS/Solar Physics Division Meeting*
- Casimir, H. B. G. 1963, *On the Interaction Between Atomic Nuclei and Electrons* (San Francisco: Freeman)
- Collados, M., Bettonvil, F., Cavaller, L., et al. 2010, in *Society of Photo-Optical Instrumentation Engineers (SPIE) Conference Series*, Vol. 7733, *Society of Photo-Optical Instrumentation Engineers (SPIE) Conference Series*
- Collados, M., Bettonvil, F., Cavaller, L., et al. 2013, in *Highlights of Spanish Astrophysics VII*, ed. J. C. Guirado, L. M. Lara, V. Quilis, & J. Gorgas, 808–819
- de la Cruz Rodríguez, J., De Pontieu, B., Carlsson, M., & Rouppe van der Voort, L. H. M. 2013a, *ApJ*, 764, L11
- de la Cruz Rodríguez, J. & Piskunov, N. 2013, *ApJ*, 764, 33
- de la Cruz Rodríguez, J., Rouppe van der Voort, L., Socas-Navarro, H., & van Noort, M. 2013b, *A&A*, 556, A115
- de la Cruz Rodríguez, J., Socas-Navarro, H., Carlsson, M., & Leenaarts, J. 2012, *A&A*, 543, A34
- De Pontieu, B., Title, A. M., Lemen, J. R., et al. 2014, *Sol. Phys.*, 289, 2733
- Denker, C., Lagg, A., Puschmann, K. G., et al. 2012, *IAU Special Session*, 6
- Dragon, J. N. & Mutschlecner, J. P. 1980, *ApJ*, 239, 1045
- Gingerich, O., Noyes, R. W., Kalkofen, W., & Cuny, Y. 1971, *Sol. Phys.*, 18, 347
- Goode, P. R. & Cao, W. 2012, in *Society of Photo-Optical Instrumentation Engineers (SPIE) Conference Series*, Vol. 8444, *Society of Photo-Optical Instrumentation Engineers (SPIE) Conference Series*
- Gudiksen, B. V., Carlsson, M., Hansteen, V. H., et al. 2011, *A&A*, 531, A154
- Hayek, W., Asplund, M., Carlsson, M., et al. 2010, *A&A*, 517, A49
- Katsukawa, Y., Watanabe, T., Hara, H., et al. 2012, *IAU Special Session*, 6
- Keil, S. L., Rimmele, T., Keller, C. U., et al. 2003, in *Innovative Telescopes and Instrumentation for Solar Astrophysics*. Edited by Stephen L. Keil, Sergey V. Avakyan . *Proceedings of the SPIE*, Volume 4853, pp. 240-251 (2003)., 240–251
- Keil, S. L., Rimmele, T. R., Wagner, J., Elmore, D., & ATST Team. 2011, in *Astronomical Society of the Pacific Conference Series*, Vol. 437, *Solar Polarization 6*, ed. J. R. Kuhn, D. M. Harrington, H. Lin, S. V. Berdyugina, J. Trujillo-Bueno, S. L. Keil, & T. Rimmele, 319
- Khomenko, E., Collados, M., Diaz, A., & Vitas, N. 2014, *ArXiv e-prints*
- Kostik, R. I., Shchukina, N. G., & Rutten, R. J. 1996, *A&A*, 305, 325
- Landi Degl'Innocenti, E. & Landolfi, M. 2004, *Polarization in Spectral Lines* (Kluwer Academic Publishers)
- Leenaarts, J. & Carlsson, M. 2009, in *Astronomical Society of the Pacific Conference Series*, Vol. 415, *The Second Hinode Science Meeting: Beyond Discovery-Toward Understanding*, ed. B. Lites, M. Cheung, T. Magara, J. Mariska, & K. Reeves, 87
- Leenaarts, J., Carlsson, M., & Rouppe van der Voort, L. 2012, *ApJ*, 749, 136
- Leenaarts, J., de la Cruz Rodríguez, J., Kochukhov, O., & Carlsson, M. 2014, *ApJ*, 784, L17
- Mihalas, D. 1974, *Sol. Phys.*, 35, 11
- Nahar, S. N. & Pradhan, A. K. 1994, *Journal of Physics B: Atomic, Molecular and Optical Physics*, 27, 429
- Olson, G. L. & Kunasz, P. B. 1987, *J. Quant. Spec. Radiat. Transf.*, 38, 325
- Pereira, T. M. D., Leenaarts, J., De Pontieu, B., Carlsson, M., & Uitenbroek, H. 2013, *ApJ*, 778, 143
- Pevtsov, A. A., Streander, K., Harvey, J., et al. 2011, in *AAS/Solar Physics Division Abstracts #42*, 1747
- Rees, D. E. 1969, *Sol. Phys.*, 10, 268
- Rees, D. E., Durrant, C. J., & Murphy, G. A. 1989, *ApJ*, 339, 1093
- Rempel, M. & Schlichenmaier, R. 2011, *Living Reviews in Solar Physics*, 8, 3
- Ruiz Cobo, B. & del Toro Iniesta, J. C. 1992, *ApJ*, 398, 375
- Sánchez Almeida, J. & Trujillo Bueno, J. 1999, *ApJ*, 526, 1013
- Scharmer, G. & Carlsson, M. 1985, *Journal of Computational Physics*, 50, 56
- Scharmer, G. B., Bjelksjo, K., Korhonen, T. K., Lindberg, B., & Petterson, B. 2003, in *Society of Photo-Optical Instrumentation Engineers (SPIE) Conference Series*, Vol. 4853, *Innovative Telescopes and Instrumentation for Solar Astrophysics*, ed. S. L. Keil & S. V. Avakyan, 341–350
- Scharmer, G. B., Narayan, G., Hillberg, T., et al. 2008, *ApJ*, 689, L69
- Shimizu, T., Tsuneta, S., Hara, H., et al. 2011, in *Society of Photo-Optical Instrumentation Engineers (SPIE) Conference Series*, Vol. 8148, *Society of Photo-Optical Instrumentation Engineers (SPIE) Conference Series*
- Socas-Navarro, H. 2003, *Neural Networks*, 16, 355
- Socas-Navarro, H. 2005, *ApJ*, 621, 545
- Socas-Navarro, H. 2011, *A&A*, 529, A37
- Socas-Navarro, H. 2014, *A&A*, *in preparation*
- Socas-Navarro, H., Ruiz Cobo, B., & Trujillo Bueno, J. 1998, *ApJ*, 507, 470
- Socas-Navarro, H. & Trujillo Bueno, J. 1997, *ApJ*, 490, 383
- Socas-Navarro, H., Trujillo Bueno, J., & Ruiz Cobo, B. 2000, *ApJ*, 530, 977
- Soltau, D., Volkmer, R., von der Lühe, O., & Berkefeld, T. 2012, *Astronomische Nachrichten*, 333, 847
- Stein, R. F. 2012, *Living Reviews in Solar Physics*, 9, 4
- Trujillo Bueno, J. 2003, in *Astronomical Society of the Pacific Conference Series*, Vol. 288, *Stellar Atmosphere Modeling*, ed. I. Hubeny, D. Mihalas, & K. Werner, 551
- Trujillo Bueno, J. & Landi Degl'Innocenti, E. 1996, *Sol. Phys.*, 164, 135
- Uitenbroek, H. 1989, *A&A*, 213, 360
- Uitenbroek, H. 2001, *ApJ*, 557, 389
- Unsold, A. 1955, *Physik der Sternatmosphären*, MIT besonderer Berücksichtigung der Sonne.
- Štěpán, J. & Trujillo Bueno, J. 2013, *A&A*, 557, A143
- van Noort, M., Hubeny, I., & Lanz, T. 2002, *ApJ*, 568, 1066
- Wittmann, A. 1974, *Sol. Phys.*, 35, 11